Journal Name

ARTICLE

Porous $NiTiO_3/TiO_2$ Nanostructures for Photocatatalytic Hydrogen Evolution

Received 00th January 20xx,
Accepted 00th January 20xx

DOI: 10.1039/x0xx00000x

www.rsc.org/

Congcong Xing,[ab] Yongpeng Liu,[c] Yu Zhang,[a] Junfeng Liu,[a] Ting Zhang,[d] Pengyi Tang,[d] Jordi Arbiol,[de] Lluís Soler,[b] Kevin Sivula,[c] Néstor Guijarro,[c] Junshan Li,[a] Ruifeng Du,[a] Yong Zuo,[a] Andreu Cabot,*[ae] Jordi Llorca *[b]

We present a strategy to produce porous $NiTiO_3/TiO_2$ nanostructures with excellent photocatalytic activity toward hydrogen generation. In a first step, nickel-doped TiO_2 needle bundles were synthesized by a hydrothermal procedure. Through the sintering in air of these nanostructures, porous $NiTiO_3/TiO_2$ heterostructured rods were obtained. Alternatively, the annealing in argon of the nickel-doped TiO_2 needle bundles resulted in NiO_x/TiO_2 elongated nanostructures. Porous $NiTiO_3/TiO_2$ structures were tested for hydrogen evolution in the presence of ethanol. Such porous heterostructures exhibited superior photocatalytic activity toward hydrogen generation, with hydrogen production rates up to 11.5 $mmol \cdot h^{-1} \cdot g^{-1}$ at room temperature. This excellent performance is related here with the optoelectronic properties and geometric parameters of the material.

Introduction

Since first reports on photocatalytic water splitting, TiO_2 has been considered one of the most attractive photocatalysts.[1-3] Among others, its interest resides on its excellent optoelectronic properties, high resistance to photocorrosion, natural abundance, low-cost and safety.[4-6] However, TiO_2 optimization for solar photocatalysis requires maximizing its surface area.[7] It also requires the introduction of dopants, additional phases or structural defects that allow this wide band gap semiconductor to take advantage of a larger spectral range of the solar radiation.[8-13]

To maximize surface area, the production of hollow and porous TiO_2 nanostructures has recently drawn growing attention.[14-16] Besides, Ti-based mixed oxides and particularly perovskite titanates $MTiO_3$ (M=Ba, Sr, Ca and Ni) have been pointed out as a new exciting class of photoactive materials.[17-19] Additionally heterostructured oxides, such as $SrTiO_3/TiO_2$ and $NiTiO_3/TiO_2$ have been demonstrated to promote charge-separation, hole-transportation and visible-light-driven photocatalytic performance over TiO_2.[20-22] However, the synthesis of such mixed oxides in the form of high surface area materials is extremely challenging, what has limited advances in this direction.[23-27]

To overcome this severe challenge, we present here a simple, high throughput and scalable hydrothermal-based strategy to produce porous $NiTiO_3/TiO_2$ heterostructures. This strategy is based on the synthesis of needle bundles of Ni-doped TiO_2 (TiO_2:Ni) and their posterior sintering in air to produce highly crystalline $NiTiO_3/TiO_2$ heterostructures with a significant level of porosity reminiscent of the large density of interfaces within the needle bundles. We further demonstrate here that these preliminarily optimized materials are excellent photocatalysts for hydrogen generation.

Experimental

Chemicals

Titanium(IV) isopropoxide (97%, Sigma-Aldrich), nickel(II) nitrate hexahydrate (98%, Fluka), ethanol (96%, PanReac AppliChem), hexadecylamine (HDA, 90%, Sigma-Aldrich), potassium chloride (Sigma-Aldrich), and ammonium hydroxide solution (28-30%, Sigma-Aldrich) were used without further purification.

Synthesis of $NiTiO_3/TiO_2$ Heterostructures

A solution of KCl (1.9 mg) in miliQ water (0.99 g) was added dropwise to a HDA (0.45 g) solution in ethanol (20 mL) under stirring at room temperature. To this solution, a proper amount of $Ni(NO_3)_2 \cdot 6H_2O$ was added (0 mg, 22.5 mg, 45 mg, 90 mg, and 225 mg to reach 0, 0.5, 1, 2, and 5 mol% concentrations, respectively). Then, 4.7 mL of titanium(IV) isopropoxide was

[a] Catalonia Institute for Energy Research (IREC), Sant Adrià de Besòs, 08930 Barcelona, Spain
[b] Institute of Energy Technologies, Department of Chemical Engineering and Barcelona Research Center in Multiscale Science and Engineering, Universitat Politècnica de Catalunya, EEBE, 08019 Barcelona, Spain
[c] Laboratory for Molecular Engineering of Optoelectronic Nanomaterials (LIMNO), École Polytechnique Fédérale de Lausanne (EPFL), Station 6, CH-1015 Lausanne, Switzerland
[d] Catalan Institute of Nanoscience and Nanotechnology (ICN2), CSIC and BIST, Campus UAB, Bellaterra, 08193 Barcelona, Catalonia, Spain
[e] ICREA, Pg. Lluis Companys 23, 08010 Barcelona, Spain

† Electronic Supplementary Information (ESI) available: additional TEM, HRTEM, EELS analysis and other characterizations, photocatalytic hydrogen production measurement. See DOI: 10.1039/x0xx00000x

added. After stirring for 1 h at room temperature, we kept the solution 16 h without stirring, and afterward the solution was washed with ethanol three times using centrifugation to recover the product. This product was then dissolved in a solution containing 20 mL of MiliQ water, 40 mL of ethanol and 2.2 mL of ammonium hydroxide. This solution was stirred for 1 h and it was subsequently transferred to a 100mL Teflon-lined hydrothermal reactor. The reactor was heated at 170 °C and maintained at this temperature for 17 h. Afterward, it was cooled down to room temperature and the product was washed three times with ethanol. Dried materials were finally annealed in a tube furnace under synthetic air flow at 650 °C for 8 h.

Characterization

X-ray diffraction analyses (XRD, 2θ: 20º-80º; scanning rate: 5º/min) were carried out on a Bruker AXS D8 Advance X-ray diffractometer with Ni-filtered Cu-Kα radiation (λ= 0.15406 Å), operating at 40 mA and 40 kV. The morphology and size of the particles were characterized by transmission electron microscopy (TEM, ZEISS LIBRA 120), working at 120 kV and field-emission scanning electron microscopy (SEM, Zeiss Auriga) operating at 5.0 kV. High resolution transmission electron microscopy (HRTEM) images and scanning transmission electron microscopy (STEM) studies were conducted on a FEI Tecnai F20 field emission gun microscope operated at 200 kV with a point-to-point resolution of 0.19 nm, which was equipped with high angle annular dark field (HAADF) and a Gatan Quantum electron energy loss spectroscopy (EELS) detectors. Elemental analysis was carried out using an Oxford energy dispersive X-ray spectrometer (EDX) combined with the Zeiss Auriga SEM working at 20.0 kV. X-ray photoelectron spectroscopy (XPS) was examined on a SPECS system equipped with a Phoibos 150 MCD-9 detector, working at 150 mW with an Al anode XR50 source. Fourier transform infrared spectroscopy (FTIR, Alpha Bruker) was carried with a platinum attenuated total reflectance single reflection module.

Photocatalytic Hydrogen Evolution Tests

In a typical experiment, a cellulose paper impregnated with 2.0 mg of the photocatalyst was placed inside a photocatalytic reactor that was equipped with a UV LED (Figure S1). An Ar gas stream was saturated with a water:ethanol vapour mixture (90:10 ratio on a molar basis) by bubbling dry Ar gas at a flow rate of 20 mL·min^{-1} through a saturator (Dreschel bottle) containing a liquid mixture of 87.5 g of H_2O and 9.92 g of ethanol.[28-31] This Ar stream was introduced into the photoreactor and passed through the cellulose paper loaded with the photocatalyst. The photoreactor effluent was monitored on-line every 4 min using gas chromatography (GC) (Agilent 3000A MicroGC) using three columns: MS 5 Å, Plot U and Stabilwax. The LED UV light source (from SACOPA, S.A.U.) consisted of four LEDs at 365 ± 5 nm and a synthetic quartz glass cylindrical lens that transmitted the light to the photocatalyst. Light irradiation was measured directly with a UV-A radiation monitor from Solar Light Co. and was 79.1± 0.5 mW·cm^{-2} at the sample position. At the beginning of each experiment, the UV light was off, and the reaction system was purged by entering 20 mL·min^{-1} of saturated Ar gas with the water-ethanol vapour mixture, to remove oxygen in the line. After 30 min, the UV light was turned on and we monitored all photoreaction products during ca. 20-40 min by GC. Control experiments were carried out with only the cellulose paper support and no photoactivity was measured.

Electrochemical Impedance Spectroscopy (EIS)

EIS analyses were performed using a Bio-Logic SP-300 potentiostat in a 3-electrode configuration employing a Cappuccino-type PEC cell, wherein the photocatalyst was deposited as a thin film in a conductive substrate (FTO) to be used as working electrode, whereas a Ag/AgCl electrode and a Pt wired were used as a reference and a counter electrode, respectively. The applied potential on the working electrode was sinusoidally modulated with an amplitude of 25 mV using frequencies ranging from 100 kHz to 50 mHz. The analysis of the impedance response was undertaken using ZView (Scribner Associates).

Results and discussion

Characterization of the Photocatalysts

Ni-doped TiO_2 (TiO_2:Ni) nanostructures were produced from the hydrothermal decomposition of titanium(IV) isopropoxide in the presence of proper amounts of nickel(II) nitrate hexahydrate, HDA as a shape-directing agent and KCl to control the ionic strength of the solution (see experimental section for details and Figure S2 for SEM images).[32] As shown by TEM characterization, the size and shape of the nanostructures obtained from this hydrothermal reaction strongly depended on the amount of Ni introduced (Figure S3). In the absence of Ni, nanoparticles with an average size around 50 nm and mostly irregular shapes, although some elongated, were obtained. When introducing increasingly higher amounts of Ni, more and more elongated nanostructures were obtained. In the presence of a nominal 5% of Ni, most structures resembled nanorods with a length in the range from 100 nm to 200 nm and thickness of 30-60 nm (Figures 1b, 2b and S3). A closer look to these nanorods allowed discerning that they consisted of needle-shaped nanostructures assembled in bundles (Figure 2b).

XRD analyses showed the crystal structure of these needle bundles to match that of anatase TiO_2. Diffraction peaks shifted to lower angles with the introduction of increasing amounts of Ni (Figure 1a), which pointed at the presence of Ni ions within the TiO_2 anatase lattice. Besides anatase TiO_2, no additional crystallographic phase could be discerned from XRD patterns. EDX analysis showed the Ni atomic concentration to be systematically higher than the nominal amount introduced, pointing at a higher yield of reaction of the nickel(II) nitrate than the titanium(IV) isopropoxide under the hydrothermal conditions used for the synthesis (Table S1).

TiO_2:Ni nanopowders were annealed under synthetic air flow at 650 °C during 8 h. Upon this thermal treatment, the color of the material changed from the original blueish,

characterizing TiO_2:Ni samples, to yellow (Figure S4). TEM micrographs of the annealed powder showed it to still consist on elongated nanostructures. However, on the contrary to the starting nanoneedle bundles, the annealed nanostructures displayed a crystallographic continuity (Figure 2c). Additionally, the annealed nanostructures presented numerous holes all over them (Figure 2d). In contrast, the annealing of undoped TiO_2 nanopowders in the same conditions did not result in such porous structure (Figure S5).

XRD analysis showed that the porous nanostructures obtained after the annealing of TiO_2:Ni in air consisted mainly on anatase TiO_2 (Figure 2a, S6). With the annealing process, the shift of the XRD peaks observed in the precursor TiO_2:Ni material disappeared, pointing at the outward diffusion of the Ni ions from the TiO_2 lattice. Besides the anatase phase, XRD patterns displayed the presence of a second crystal structure, which was identified as $NiTiO_3$.[33] The relative intensity of the peaks associated to this $NiTiO_3$ phase clearly increased with the nominal amount of Ni (Figure 2a). Rietveld analysis showed the relative amount of the $NiTiO_3$ phase to correspond to a 4.6 mol%, 9.0 mol% and 15 mol%, for samples obtained from nominal Ni concentration of 1 mol%, 2 mol% and 5 mol%, respectively (Figure S7).[34] Within its experimental error, EDX analysis showed the Ni molar concentrations to be maintained after the annealing process (Table S1).

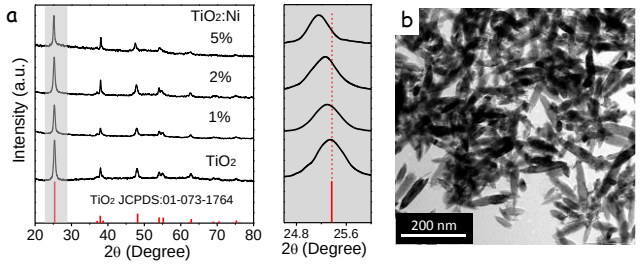

Figure 1. a) XRD patterns of TiO_2 and TiO_2:Ni (1%, 2%, 5%) nanopowders. b) TEM image of TiO_2:Ni (5%) nanopowder.

HRTEM analysis confirmed the annealed material to contain mostly anatase TiO_2 (Figures S5 and S6).[35] EELS elemental maps of the annealed materials showed Ni, Ti and O to be evenly distributed throughout the nanostructures (Figure 2e, S5). The lack of evidences of the presence of large $NiTiO_3$ crystal domains and the homogeneous distribution of Ni throughout the material observed by EELS and EDX analyses pointed at the growth of small $NiTiO_3$ domains as a discontinuous shell on the surface of the porous TiO_2 nanostructures.[36] XPS analyses of the annealed samples displayed only one chemical state for Ti, assigned to Ti^{4+}, and one for Ni, assigned to Ni^{2+}, consistently with XRD, HRTEM, EELS and EDX characterization (Figures S8 and S9).[37] XPS analysis showed the amount of Ni to be almost a twofold of that measured by EDX, pointing at its preferential surface location (Table S1).

When the Ni-doped material was annealed under Ar instead of air, the sample color changed from blue to black, instead of yellow (Figure S4), but the elongated geometry of the annealed structures was conserved. In contrast to the annealing in air, the nanostructuration of the original nanoneedle bundles partially persisted after annealing in argon. The particles annealed in argon did not show full crystallographic continuity and contained a lower density of holes compared with the material obtained from the annealing in air (Figure S10). XRD patterns of materials annealed under argon showed anatase TiO_2 as the main phase, with no evidence of the presence of $NiTiO_3$, but with a small XRD peak at $2\theta=28.6°$ that we associated to a NiO_x phase (Figure S11). The black nanopowder annealed under argon showed a magnetic moment, which further pointed toward the formation of a NiO_x phase (Figure S4).[38]

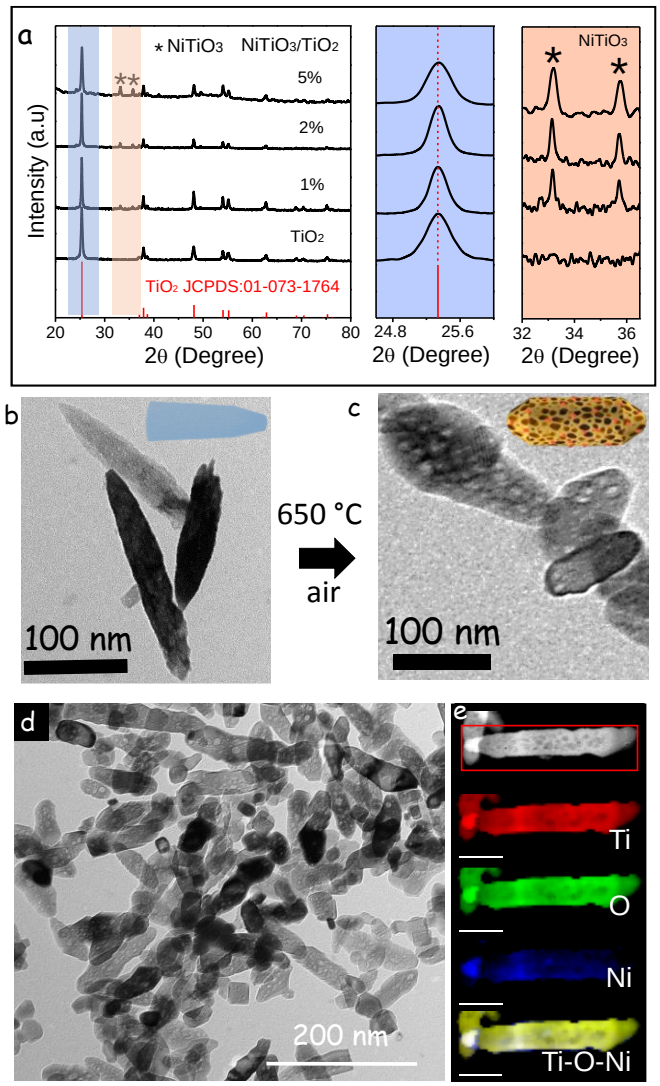

Figure 2. a) XRD patterns of $NiTiO_3/TiO_2$ (0, 1%, 2%, 5%) nanopowders obtained after annealing in air. b) TEM micrograph of TiO_2:Ni (5%) needle bundles. c, d) TEM micrographs of $NiTiO_3/TiO_2$ (5%) porous structures obtained after annealing in air. e) HAADF micrograph of a $NiTiO_3/TiO_2$ (5%) rod and corresponding EELS elemental maps for Ti, O, Ni and Ti-O-Ni.

We hypothesize that the porous geometry of the $NiTiO_3/TiO_2$ structures obtained after annealing TiO_2:Ni in air was created by the sintering of the nanoneedle bundles. The large density of interfaces of the initial bundles translated in the formation of a large density of holes on the sintered material, which could be aided by the simultaneous outward diffusion of

Ni ions to form $NiTiO_3$ domains. On the contrary, annealing in argon did not allow a similar level of sintering of the nanostructures, which was promoted in air by the ubiquitous presence of oxygen. Thus, the material obtained from the annealing process in argon maintained smaller crystal domains and presented a less porous structure. With the annealing process in air, pure TiO_2 nanopowders did not result in porous materials as those obtained from TiO_2:Ni because they did not present a proper initial nanostructuration.

Photogeneration of Hydrogen

To test their photocatalytic properties toward hydrogen evolution, the annealed materials were supported on a conventional filter paper and placed on a reactor containing a UV LED light source. An Ar flow saturated with a water-ethanol vapor mixture was flowed through this reactor. Exhaust gases were analyzed using GC, being acetaldehyde and hydrogen the main products of the reaction (see details in the experimental section and Figure S1).

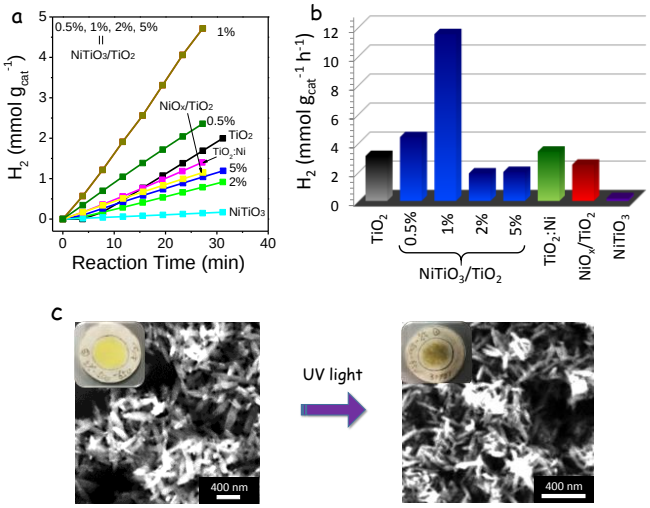

Figure 3. a) H_2 production of TiO_2, $NiTiO_3/TiO_2$ (1%, 2%, 5%), NiO_x/TiO_2 (1%) and $NiTiO_3$. b) H_2 production rate of TiO_2, $NiTiO_3/TiO_2$ (1%, 2%, 5%), NiO_x/TiO_2 (1%) and $NiTiO_3$. c) Optical and SEM images of $NiTiO_3/TiO_2$ (5%) before and after 30 min photocatalytic test.

Figure 3a shows the accumulated hydrogen production during a 32 min reaction for $NiTiO_3/TiO_2$ hetero-nanostructures having different nominal Ni concentrations. Data for bare TiO_2 and pure $NiTiO_3$ prepared following the same procedure (see experimental section for details) were also plotted in Figure 3a as reference. $NiTiO_3/TiO_2$ hetero-nanostructures with a nominal 1% of Ni systematically provided the highest hydrogen production rates, with values up to 11.5 $mmol \cdot h^{-1} g^{-1}$, well above those previously reported for other Ni-Ti-O systems (Table S2). The hydrogen production rate of $NiTiO_3/TiO_2$ (1%) was almost a fourfold higher than that of bare TiO_2 and 60 times larger than that of pure $NiTiO_3$ (Figure 3b, S12, S13, S14). The presence of larger amounts of Ni did not improve the evolution rate with respect to $NiTiO_3/TiO_2$ (1%). We associate this experimental evidence with the blocking of the TiO_2 surface active sites when too large amounts of $NiTiO_3$ were grown on the TiO_2 surface. SEM characterization showed the morphology of the $NiTiO_3/TiO_2$ hetero-nanostructures to remain unmodified after the catalytic test (Figure 3c).

We believe the enhancement of the photocatalytic properties of TiO_2 with the $NiTiO_3$ introduction to be related with an improvement of three fundamental parameters: i) surface area; ii) light absorption; and iii) charge separation. We estimate that the introduction of Ni had associated a factor 3 increase of the surface area with respect to pure TiO_2 through the formation of the porous $NiTiO_3/TiO_2$ hetero-nanostructures during the annealing process. Additionally, the presence of $NiTiO_3$ provided a higher light absorption coefficient at the used excitation wavelength (Figure S15). In case of using solar radiation, the presence of $NiTiO_3$ would provide an even larger improvement with respect to pure TiO_2, as it would allow absorbing a larger portion of the solar spectra due to its smaller band gap. Besides, the proper band alignment of TiO_2 and $NiTiO_3$ allowed an efficient spatial charge separation that significantly reduced recombination of the photogenerated charge carriers before reaction.

To gain additional insight into the band structure alignment and the interfacial charge carrier dynamics at the $NiTiO_3/TiO_2$ heterostructure, EIS analyses were carried out on TiO_2, $NiTiO_3/TiO_2$ (1%) and $NiTiO_3$ thin films in dark conditions. Representative impedance responses in the form of Nyquist plot for TiO_2 and $NiTiO_3/TiO_2$ (1%) are displayed in Figure 4a. Responses typically feature a single semicircle. Interestingly, the size of the semicircle obtained for the TiO_2 sample was reduced with the incorporation of Ni. A more quantitative description of the EIS data can be provided by modelling the electrical response with an equivalent circuit, such as a Randles circuit (Figure 4a inset), which has been previously reported to successfully describe nanostructured TiO_2 and other photocatalysts.[22,39] This circuit consists of a resistor R_S in series with a bulk capacitance C_{bulk}, attributed to the space charge region, and a second resistor $R_{ct,bulk}$ that represents the charge transport resistance, both in parallel. At a first glance, the decrease in the size of the semicircle with the incorporation of Ni in TiO_2 suggests the reduction in the charge transport resistance,[39,40] which is further confirmed with the decrease of $R_{ct,bulk}$ from 15.4 kΩ to 9.8 kΩ pointing out the amelioration of the charge transport process. In addition, the electron lifetime τ_n can be calculated as the inverse of the angular frequency at the maximum of the Nyquist plot ($2\pi f_{max}$),[22] highlighted in Figure 4a. Results reveal that τ_n increases from 4.5 ms to 6.6 ms when the heterostructure is formed. In general, τ_n is considered a metric of electron recombination, *i.e.*, the longer the value the lesser the charge recombination. The lengthening of τ_n when TiO_2 is interfaced with $NiTiO_3$ underpins the effective charge carrier separation across the n-n heterojunction and thus the enhanced photocatalytic activity of the composite with respect TiO_2. Similar behavior has recently been reported by Wei and co-workers on $NiTiO_3/TiO_2$ composite for inorganic sensitized solar cells.[22]

In an attempt to further interrogate the energy band positions, Mott–Schottky (M–S) plots were constructed from

C_{bulk} values extracted from EIS measurements on TiO_2 and $NiTiO_3$ and further analyzed using the M–S equation:

$$C_{bulk}^{-2} = \frac{2}{qA^2\varepsilon\varepsilon_0 N_D}\left(V - V_{fb} - \frac{kT}{q}\right)$$

where q is elementary charge, A is taken as the geometric area (assuming a low surface roughness spin-coated thin film), ε is relative permittivity (taken to be 55 and 15 for TiO_2[41] and $NiTiO_3$,[42] respectively), ε_0 is vacuum permittivity, N_D is donor density, V is applied potential, V_{fb} is flat band potential, k is Boltzmann constant, and T is absolute temperature. The positive slope in the linear region (dashed line in Figure 4b) unambiguously confirmed the n-type character of both $NiTiO_3$ and TiO_2, whereas V_{fb} values of –0.186 V and –0.276 V *vs.* RHE were obtained for TiO_2 and $NiTiO_3$, respectively. Likewise, N_D shows values of 1.1×10^{18} cm^{-3} for TiO_2 and 5.5×10^{17} cm^{-3} for $NiTiO_3$. Similar values have also been reported by Thimsen et al. on nanocrystalline anatase TiO_2,[42] and by Trari and co-workers on nanostructured $NiTiO_3$.[43] We note that the depletion width is estimated to be 20 nm in the linear region of M–S plot for both TiO_2 and $NiTiO_3$ so that M–S analysis can be reasonably applied in the case of not fully depleted feature.[44] Considering the density-of-state effective mass for electrons m_{de} for nanocrystalline anatase TiO_2 is 9.1×10^{-30} kg,[41] and for nanostructured $NiTiO_3$ is 1.9×10^{-30} kg,[44] the effective density of states in the conduction band N_C is given by:[44,47]

$$N_C \equiv 2\left(\frac{2\pi m_{de} kT}{h^2}\right)^{\frac{3}{2}}$$

where h is Planck constant. N_C is estimated to be 7.7×10^{20} cm^{-3} for TiO_2, and 7.5×10^{19} cm^{-3} for $NiTiO_3$. Since the ratio between N_D and N_C is in all cases less than 0.05, both TiO_2 and $NiTiO_3$ could be treated as nondegenerate semiconductors, and therefore, the Boltzmann statistics can be applied:[44,47]

$$E_{CB} - E_F = kT\ln\left(\frac{N_C}{N_D}\right)$$

where E_{CB} is the bottom of the conduction band and E_F is the Fermi level position. E_{CB} is found to be around 168 mV and 126 mV above V_{fb} for TiO_2 and $NiTiO_3$, respectively. Based on the aforementioned calculations, a scheme of the electronic band structures is illustrated in Figure 4c, where the relative band alignment between $NiTiO_3$ and TiO_2 allows for efficient charge transfer. In such Ni-TiO_2 system, photogenerated electrons in the conduction band of $NiTiO_3$ could transfer to the conduction band of TiO_2 to promote water reduction while photogenerated holes in TiO_2 could migrate to $NiTiO_3$ to drive ethanol dehydrogenation to acetaldehyde and hydrogen. Therefore, the formation of $NiTiO_3/TiO_2$ n-n junction can effectively suppress the electron-hole recombination process within TiO_2. As a result, $NiTiO_3/TiO_2$ composites at optimal $NiTiO_3$ loading condition shows a significant increased photocatalytic activity. In fact, incorporating $NiTiO_3$ in other semiconductor photoabsorber materials such as TiO_2,[22] α-Fe_2O_3[47] and Ag_3VO_4[18] has also shown to enhance the charge separation efficiency.

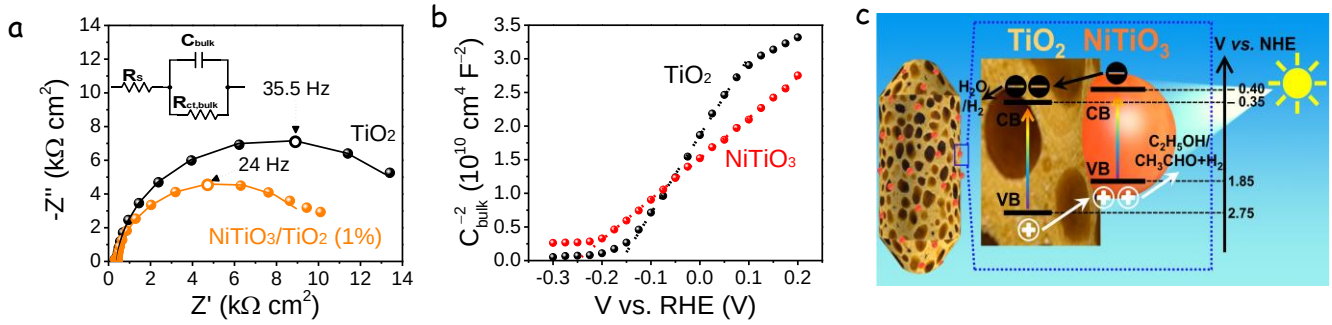

Figure 4. a) Representative impedance response of TiO_2 (black sphere) and $NiTiO_3/TiO_2$ (1%) (orange sphere) with the corresponding fit (solid lines) in Nyquist plot. The maximum point of the Nyquist plot is highlighted (hollow), and the equivalent circuit used is included as an inset. b) Mott–Schottky plot of TiO_2 (black sphere) and $NiTiO_3$ (red sphere) including a linear fit (dashed lines). c) Schematics of the electronic band structures of $NiTiO_3/TiO_2$ n-n heterojunction.

Conclusions

Porous $NiTiO_3/TiO_2$ heterostructures were prepared from the annealing in air of TiO_2:Ni nanoneedle bundles obtained from a hydrothermal route. Pores were generated during the sintering of the nanostructured bundles due to the presence of a large density of interfaces on the precursor material. $NiTiO_3/TiO_2$ heterostructures were used for photocatalytic hydrogen generation from ethanol-water solutions at room temperature. $NiTiO_3/TiO_2$ hetero-structures provided unprecedented H_2 production rates up to 11.5 $mmol\cdot h^{-1}g^{-1}$. This was associated to the improvement of three parameters, sur-face area, light absorption and charge separation. We estimated a factor 3 increase of the surface area with the introduction of Ni through the formation of porous $NiTiO_3/TiO_2$ hetero-nanostructures during the annealing in air. Additionally, the pres-ence of $NiTiO_3$, with a lower band gap energy, provided a higher light absorption coefficient at the excitation wavelength. Besides,

TiO_2 and $NiTiO_3$ presented a proper band alignment that allows an efficient spatial charge separation of the photogenerated charge carriers before reaction, as confirmed by EIS analysis.

Conflicts of interest

There are no conflicts of interest to declare.

Acknowledgements

This work was supported by the European Regional Development Funds and by the Spanish Ministerio de Economía y Competitividad through project SEHTOP (ENE2016-77798-C4-3-R and ENE2015-63969-R). Y.L. and N.G. thank the Swiss National Science Foundation (SNF) for funding under the Ambizione Energy grant no. PZENP2_166871. J.L. is a Serra Hunter fellow and is grateful to ICREA Academia program and GC 2017 SGR 128. T.Z., P.Y.T. and J.A. acknowledge funding from Generalitat de Catalunya 2017 SGR 327 and the Spanish MINECO project ENE2017-85087-C3. ICN2 acknowledges support from the Severo Ochoa Programme (MINECO, Grant no. SEV-2013-0295) and is funded by the CERCA Programme / Generalitat de Catalunya. Part of the present work has been performed in the framework of Universitat Autònoma de Barcelona Materials Science PhD program. C.C.X., Y.Z and T.Z. thank the China Scholarship Council for scholarship support.

Notes and references

1 X. Wu, G. Q. Lu and L. Wang, *Energy Environ. Sci.*, 2011, **4**, 3565–3572.
2 D. P. Wang and H. C. Zeng, *Chem. Mater.*, 2009, **21**, 4811–4823.
3 Q. Xiang, J. Yu and M. Jaroniec, *J. Am. Chem. Soc.,* 2012, **134**, 6575–6578.
4 Y. Ma, X. Wang, Y. Jia, X. Chen, H. Han and C. Li, *Chem. Rev.*, 2014, **114**, 9987–10043.
5 D. Su, S. Dou and G. Wang, *Chem. Mater.*, 2015, **27**, 6022–6029.
6 J. Liu, H. Bai, Y. Wang, Z. Liu, X. Zhang and D. D. Sun, *Adv. Funct. Mater.*, 2010, **20**, 4175–4181.
7 B. Liu and H. C. Zeng, *Chem. Mater.*, 2008, **20**, 2711–2718.
8 N. O. Gopal, H. H. Lo and S. C. Ke, *J. Am. Chem. Soc.*, 2008, **130**, 2760–2761.
9 C. Burda, Y. Lou, X. Chen, A. C. S. Samia, J. Stout and J. L. Gole, *Nano Lett.*, 2003, **3**, 1049–1051.
10 M. Chiodi, C. P. Cheney, P. Vilmercati, E. Cavaliere, N. Mannella, H. H. Weitering and L. Gavioli, *J. Phys. Chem. C*, 2012, **116**, 311–318.
11 R. Bouchet, A. Weibel, P. Knauth, G. Mountjoy and A. V. Chadwick, *Chem. Mater.*, 2003, **15**, 4996–5002.
12 M. Murdoch, G. I. N. Waterhouse, M. A. Nadeem, J. B. Metson, M. A. Keane, R. F. Howe, J. Llorca and H. Idriss, *Nat. Chem.*, 2011, **3**, 489–492.
13 G. I. N. Waterhouse, A. K. Wahab, M. Al-Oufi, V. Jovic, D. H. Anjum, D. Sun-Waterhouse, J. Llorca and H. Idriss, *Sci. Rep.*, 2013, **3**, 2849.
14 J. H. Pan, X. Zhang, A. J. Du, D. D. Sun and J. O. Leckie, *J. Am. Chem. Soc.*, 2008, **130**, 11256–11257.
15 S. C. Yang, D. J. Yang, J. Kim, J. M. Hong, H. G. Kim, I. D. Kim and H. Lee, *Adv. Mater.*, 2008, **20**, 1059–1064.
16 J. Y. Hwang, H. M. Kim, S. K. Lee, J. H. Lee, A. Abouimrane, M. A. Khaleel, I. Belharouak, A. Manthiram and Y. K. Sun, *Adv. Energy Mater.*, 2016, **6**, 1–7.
17 H. Fan, H. Li, B. Liu, Y. Lu, T. Xie and D. Wang, *ACS Appl. Mater. Interfaces*, 2012, **4**, 4853–4857.
18 B. Inceesungvorn, T. Teeranunpong, J. Nunkaew, S. Suntalelat and D. Tantraviwat, *Catal. Commun.*, 2014, **54**, 35–38.
19 X. Wang, C.-N. Xu, H. Yamada, K. Nishikubo and X.-G. Zheng, *Adv. Mater.*, 2005, **17**, 1254–1258.
20 F. Wu, Y. Yu, H. Yang, L. N. German, Z. Li, J. Chen, W. Yang, L. Huang, W. Shi, L. Wang and X. Wang, *Adv. Mater.*, 2017, **29**, 1–7.
21 Y. Qu, W. Zhou, Z. Ren, S. Du, X. Meng, G. Tian, K. Pan, G. Wang and H. Fu, *J. Mater. Chem.*, 2012, **22**, 16471–16476.
22 Y.-Y. Li, J.-G. Wang, H.-H. Sun and B. Wei, *ACS Appl. Mater. Interfaces*, 2018, **10**, 11580–11586.
23 S. Liu, S. Xue, W. Zhang, J. Zhai and G. Chen, *J. Mater. Chem. A*, 2014, **2**, 18040–18046.
24 J. Y. Lee, J. H. Lee, S. H. Hong, Y. K. Lee and J. Y. Choi, *Adv. Mater.*, 2003, **15**, 1655–1658.
25 J. H. Pan, C. Shen, I. Ivanova, N. Zhou, X. Wang, W. C. Tan, Q. H. Xu, D. W. Bahnemann and Q. Wang, *ACS Appl. Mater. Interfaces*, 2015, **7**, 14859–14869.
26 Y. Xin, J. Jiang, K. Huo, T. Hu and P. K. Chu, *ACS Nano*, 2009, **3**, 3228–3234.
27 S. Murcia-López, M. Moschogiannaki, V. Binas, T. Andreu, P. Tang, J. Arbiol, J. Jacas Biendicho, G. Kiriakidis and J. R. Morante, *ACS Appl. Mater. Interfaces*, 2017, **9**, 40290–40297.
28 E. Molins, M. Benito, I. Mata, L. Martínez, L. Soler and J. Llorca, *MRS Adv.*, 2017, **2**, 3499–3504.
29 L. Martínez, M. Benito, I. Mata, L. Soler, E. Molins and J. Llorca, *Sustain. Energy Fuels*, 2018, **2**, 2284–2295.
30 L. Martínez, L. Soler, I. Angurell and J. Llorca, *Appl. Catal. B Environ.*, 2019, **248**, 504–514.
31 A. May-Masnou, L. Soler, M. Torras, P. Salles, J. Llorca and A. Roig, *Front. Chem.*, 2018, **6**, 110.
32 R. Imani, R. Dillert, D. W. Bahnemann, M. Pazoki, T. Apih, V. Kononenko, N. Repar, V. Kralj-Iglič, G. Boschloo, D. Drobne, T. Edvinsson and A. Iglič, *Small*, 2017, **13**, 1700349.
33 K. Huo, Y. Li, R. Chen, B. Gao, C. Peng, W. Zhang, L. Hu, X. Zhang and P. K. Chu, *Chempluschem*, 2015, **80**, 576–582.
34 B. H. Toby and R. B. Von Dreele, *J. Appl. Cryst.*, 2013, **46**, 544–549.
35 P. D. Cozzoli, A. Kornowski and H. Weller, *J. Am. Chem. Soc.*, 2003, **125**, 14539–14548.
36 H. Bin Wu, H. H. Hng and X. W. D. Lou, *Adv. Mater.*, 2012, **24**, 2567–2571.
37 J. Huang, Y. Jiang, G. Li, C. Xue and W. Guo, *Renew. Energy*, 2017, **111**, 410–415.
38 J. H. Kim, K. Zhu, Y. Yan, C. L. Perkins and A. J. Frank, *Nano Lett.*, 2010, **10**, 4099–4104.
39 Y. Zuo, Y. Liu, J. Li, R. Du, X. Yu, C. Xing, T. Zhang, L. Yao, J. Arbiol, J. Llorca, K. Sivula, N. Guijarro and A. Cabot, *ACS Appl. Mater. Interfaces*, 2019, **11**, 6918–6926.
40 X. Zhu, N. Guijarro, Y. Liu, P. Schouwink, R. A. Wells, F. Le Formal, S. Sun, C. Gao and K. Sivula, *Adv. Mater.*, 2018, **30**, 1801612.
41 E. Thimsen, A. B. F. Martinson, J. W. Elam and M. J. Pellin, *J. Phys. Chem. C*, 2012, **116**, 16830–16840.
42 S. H. Chuang, M. L. Hsieh and D. Y. Wang, *J. Chinese Chem. Soc.*, 2012, **59**, 628–632.
43 L. Boudjellal, A. Belhadi, R. Brahimi, S. Boumaza and M. Trari, *Mater. Sci. Semicond. Process.*, 2018, **75**, 247–252.

44 Y. Liu, F. Le Formal, F. Boudoire, L. Yao, K. Sivula and N. Guijarro, *J. Mater. Chem. A*, 2019, **7**, 1669–1677.
45 M. A. Ruiz Preciado, A. Kassiba, A. Morales-Acevedo and M. Makowska-Janusik, *RSC Adv.*, 2015, **5**, 17396–17404.
46 Y. Zhang, J. Gu, M. Murugananthan and Y. Zhang, *J. Alloys Compd.*, 2015, **630**, 110–116.
47 M. Rudan, *Physics of Semiconductor Devices*, 2015.

TOC graphical abstract